Structural Basis for the Quinone Reduction in the bc 1 Complex: A Comparative Analysis of Crystal Structures of Mitochondrial Cytochrome bc 1 with Bound Substrate and Inhibitors at...

ARTICLE *in* BIOCHEMISTRY · SEPTEMBER 2003

Impact Factor: 3.02 · DOI: 10.1021/bi0341814 · Source: PubMed

7 AUTHORS, INCLUDING:

Xiugong Gao
U.S. Food and Drug Administration
35 PUBLICATIONS **753** CITATIONS

Structural Basis for the Quinone Reduction in the bc_1 Complex: A Comparative Analysis of Crystal Structures of Mitochondrial Cytochrome bc_1 with Bound Substrate and Inhibitors at the Q_i Site[†,‡]

Xiugong Gao,[§] Xiaoling Wen,[||] Lothar Esser,[§] Byron Quinn,[||] Linda Yu,[||] Chang-An Yu,[||] and Di Xia*[,§]

Laboratory of Cell Biology, Center for Cancer Research, National Cancer Institute, National Institutes of Health, Bethesda, Maryland 20892, and Department of Biochemistry and Molecular Biology, Oklahoma State University, Stillwater, Oklahoma 74078

Received January 31, 2003; Revised Manuscript Received April 28, 2003

ABSTRACT: Cytochrome bc_1 is an integral membrane protein complex essential to cellular respiration and photosynthesis. The Q cycle reaction mechanism of bc_1 postulates a separated quinone reduction (Q_i) and quinol oxidation (Q_o) site. In a complete catalytic cycle, a quinone molecule at the Q_i site receives two electrons from the b_H heme and two protons from the negative side of the membrane; this process is specifically inhibited by antimycin A and NQNO. The structures of bovine mitochondrial bc_1 in the presence or absence of bound substrate ubiquinone and with either the bound antimycin A_1 or NQNO were determined and refined. A ubiquinone with its first two isoprenoid repeats and an antimycin A_1 were identified in the Q_i pocket of the substrate and inhibitor bound structures, respectively; the NQNO, on the other hand, was identified in both Q_i and Q_o pockets in the inhibitor complex. The two inhibitors occupied different portions of the Q_i pocket and competed with substrate for binding. In the Q_o pocket, the NQNO behaves similarly to stigmatellin, inducing an iron−sulfur protein conformational arrest. Extensive binding interactions and conformational adjustments of residues lining the Q_i pocket provide a structural basis for the high affinity binding of antimycin A and for phenotypes of inhibitor resistance. A two-water-mediated ubiquinone protonation mechanism is proposed involving three Q_i site residues His^{201}, Lys^{227}, and Asp^{228}.

The quinol-cyt. *c* oxidoreductase (EC 1.10.2.2, bc_1)[1] is a dimeric integral membrane protein complex and a central component of cellular energy conservation machinery in animals, plants, and bacteria. bc_1 catalyzes ET from a quinol molecule to cyt. *c* and concomitantly translocates protons across membranes for ATP synthesis and various cellular processes (*1*−*3*). Although subunit composition varies among different organisms, all bc_1 complexes contain at least three redox-active subunits carrying four prosthetic groups: a cyt. *b* with two *b*-type hemes, b_H and b_L; a cyt. c_1 with one *c*-type heme; and an ISP containing a 2Fe−2S cluster (for review, see ref *4*). The proton-motive Q cycle mechanism (*4*, *5*) best explains experimental results on the ET pathway through the four redox centers of the bc_1 complex. The mechanism postulates two separate quinone binding sites, one for quinol oxidation (Q_o site) and the other for quinone reduction (Q_i site), and a bifurcated electron flow at the Q_o site where the first electron from the substrate quinol is transferred sequentially to the ISP, cyt. c_1, and eventually to the soluble electron acceptor cyt. *c*, whereas the second electron is transferred to hemes b_L and b_H in sequence, ending at a quinone or a semiquinone anion at the Q_i site. Two protons are released into the positive side of membranes (periplasma in prokaryotes and intermembrane space in mitochondria) for every quinol oxidized. The fully reduced quinone at the Q_i site picks up two protons from the negative side of membranes (cytoplasma in prokaryotes and matrix space in mitochondria) and presumably moves to the Q_o site for reoxidation. Thus, a complete Q cycle consumes two molecules of quinol at the Q_o site, generates one quinol molecule at the Q_i site, and translocates four protons to the positive side of the membrane.

Specific bc_1 inhibitors are divided into two classes based on their points of action: class I for Q_o site inhibitors and class II for Q_i site inhibitors. The class I inhibitors such as stigmatellin and myxothizaol inhibit electron bifurcation at the Q_o site and can be further subdivided into three subgroups on the basis of common structural features and of their effects

[†] This work was supported in part from an NIH grant (GM 30721) to C.Y.

[‡] The atomic coordinates for the native bc_1 with and without bound ubiquinone and those in the presence of inhibitors of either antimycin A_1 or NQNO have been deposited for release with publication in the Protein Data Bank with accessions numbers 1NTM, 1NTZ, 1NTK, and 1NU1, respectively.

* To whom correspondence should be addressed. Tel: (301) 435-6315. Fax: (301) 435-8188. E-mail: dixia@helix.nih.gov.

[§] National Institutes of Health.

[||] Oklahoma State University.

[1] Abbreviations: bc_1, ubiquinol cytochrome *c* oxidoreductase; cyt. *b*, cytochrome *b* subunit; cyt. c_1, cytochrome c_1 subunit; ISP, iron−sulfur protein subunit; ET, electron transfer; Q_o, quinol oxidation; Q_i, quinone reduction; QH_2, ubiquinol; b_L, low-potential *b* heme; b_H, high-potential *b* heme; 2Fe−2S, two iron two sulfur cluster of ISP; Ar−Ar, aromatic−aromatic interaction; TM, transmembrane helix; IMS, intermembrane space; HQNO, 2-heptyl-4-hydroxyquinoline *N*-oxide; NQNO, 2-nonyl-4-hydroxyquinoline *N*-oxide; MOAS, methoxy acrylate stilbene; UHDBT, 5-undecyl-6-hydroxy-4,7-dioxobenzothiazol; EPR, electron paramagnetic resonance; rmsd, root-mean-square deviation; MIM, mitochondrial inner membrane.

10.1021/bi0341814 CCC: $25.00
Published on Web 07/12/2003

Table 1: Statistics of Crystallographic Data Collection and Model Refinement

	native[a,c,f]	ubiquinone[b,c]	antimycin A_1[c]	NQNO1[d]	NQNO2[d,e]
		Data collection			
resolution (Å)	50−2.4	40−2.60	50−2.60	50−3.2	50−3.2
R_{merge}[g] (outer shell)	0.058 (0.392)	0.061 (0.520)	0.075 (0.524)	0.085 (0.679)	0.085 (0.571)
$\langle I\rangle/\langle\sigma_I\rangle$ (outer shell)	21.4 (1.1)	19.4 (1.7)	20.8 (1.9)	16.1 (1.8)	17.2 (1.8)
completeness (%) (outer shell)	85.7 (77.8)	95.2 (96.7)	98.5 (95.3)	99.7 (98.3)	98.5 (94.4)
anomalous R_{merge} (outer shell)	0.055 (0.366)	0.056 (0.458)	0.072 (0.492)		
anomalous completeness (%)	77.4 (61.5)	90.0 (89.8)	95.6 (85.3)		
unique reflections	119745	104476	107555	58833	58170
free reflections	3584	2122	3224	1742	
		Model refinement			
R_{work}/R_{free}	0.232/0.282	0.243/0.285	0.234/0.272	0.215/0.296	
R_{work}/R_{free} (outer shell)	0.48/0.49	0.31/0.35	0.47/0.49	0.29/0.38	
number of atoms	17454	17465	17456	17425	
number of residues (% complete)	2093 (0.965)	2115 (0.976)	2108 (0.973)	2104 (0.971)	
number of cofactors	4	5	5	6	
number of solvent molecules	448	206	342	2	
rmsd of bond lengths (Å)	0.015	0.021	0.019	0.019	
rmsd of bond angles (Å)	1.929	1.732	1.851	2.056	

[a] Crystal with cyt. c_1 fully oxidized. [b] Crystal with cyt. c_1 partially reduced. [c] Statistics for the data set was computed at -1σ cutoff for reflection intensity, and the data set was collected at 1.0 Å wavelength. [d] Statistics for the data set was computed at -1σ cutoff for reflection intensity, and the data set was collected at 1.2 Å wavelength. [e] Model was not refined for this data set. [f] Space group symmetry for both the native and the inhibitor bound crystals is $I4_122$. [g] R_{merge} is defined as $\sum|I_{h,i} - \langle I_h\rangle|/\sum I_{h,i}$, where $I_{h,i}$ is the intensity for ith observation of a reflection with Miller index h, and $\langle I_h\rangle$ is the mean intensity for all measured $I_{h,i}$ and Friedel pairs.

on the spectroscopic behavior of cyt. *b* and ISP (*6*−*9*). Class II inhibitors, exemplified by the antimycin A, block the ET path from heme b_H to quinone or semiquinone. Antimycin A, a natural fungicide produced by *Streptomyces sp*., acts specifically on the bc_1 complex in respiratory and photosynthetic organisms with an extraordinarily high binding affinity. In bovine bc_1, the dissociation constant of bound antimycin A reaches 32 pM (*6*). Although preliminary crystallographic analyses of the bovine bc_1−antimycin A complex were reported (*8*, *10*−*12*), no refined crystal structure has been published. NQNO, another commonly used synthetic Q_i site inhibitor and structurally dissimilar to the antimycin A, binds to bc_1 with a dissociation constant (K_d) of 64 nM and can be displaced by antimycin A (*6*, *13*). NQNO reportedly possessed inhibitory effects at the Q_o site (*14*), but it was considered as a nonspecific effect in the literature (*6*). Resistant mutations showed that antimycin A and NQNO affected different sets of Q_i site residues, suggesting that their binding sites may be different.

Atomic models of mitochondrial bc_1 from several species obtained by X-ray crystallography have led to a rapid expansion of structural knowledge of bc_1 at atomic detail (*9*−*11*, *15*, *16*). Among many important structural features, two inhibitor-binding pockets were identified within the cyt. *b* subunit: one with bound antimycin A near the b_H heme and the other with many bound Q_o site inhibitors such as the myxothiazol, stigmatellin, and famoxadone in the vicinity of the b_L heme (*8*−*11*, *16*) and were designated as the Q_i and Q_o site, respectively. Negative electron density in the isomorphous difference Fourier map between antimycin A bound and the native bc_1 crystal was tentatively interpreted as a bound ubiquinone molecule in the native bc_1 (*10*), which was replaced by the inhibitor antimycin A in the complex. More recently, a ubiquinone molecule was modeled into the Q_i site based on experimental electron density and refined for the yeast bc_1 structure in the presence of bound stigmatellin and a Fv fragment (*16*).

Mechanistically, proton uptake at the Q_i site was approached in the context of a lipid environment; two potential proton uptake pathways were proposed based on analysis of bound water molecules (*17*). Details of specific binding interactions for Q_i site inhibitors, as well as the involvement of active site residues in proton uptake, are not well-defined. Here, we report the crystallographically refined structures of bovine heart mitochondrial cyt. bc_1 in the presence or absence of the substrate ubiquinone, and in complex with inhibitors of either antimycin A_1 or NQNO at the Q_i site, and discuss the mechanisms of inhibition as well as quinone reduction and protonation at the Q_i site.

EXPERIMENTAL PROCEDURES

Protein Preparation and Crystallization. Cyt. bc_1 complex from bovine heart mitochondria was prepared as described previously (*10*, *18*). For crystallization, the bc_1 particles were subject to an additional 15-step ammonium acetate fractionation to remove impurities; pure bc_1 complex in oxidized form was recovered from the precipitates formed between 18.5 and 33.5% ammonium acetate saturation. Final product was dissolved in 50 mM Tris-HCl buffer, pH 7.8, containing 0.66 M sucrose to a protein concentration of 30 mg/mL and frozen at −80 °C until use. The concentrations of cyt. *b* and c_1 were determined spectroscopically, using millimolar extinction coefficients of 28.5 and 17.5 for cyt. *b* and c_1, respectively. The homogeneity in the redox state of bc_1 was confirmed spectrophotometrically. The fully oxidized bc_1 was prepared by the addition of oxidized cyt. *c* (Sigma) followed by ammonium acetate precipitation, whereas the partially reduced bc_1 was prepared by carefully controlling the amount of sodium ascorbate added to the bc_1 solution. Redox state for cyt. c_1 of each crystallization hanging-drop was checked prior to crystal harvest (Table 1).

Purified bc_1 complexes were adjusted to a final concentration of 20 mg/mL in a solution containing 50 mM MOPS buffer at pH 7.2, 20 mM ammonium acetate, 20% (w/v) glycerol, and either 0.1% decanoyl-*N*-methylglucamide, or 0.1% diheptanoyl phosphatidylcholine, or 0.16% sucrose monocaprate. This solution was set up for crystallization as

described in previous publications (*10*, *19*, *20*). Native crystals were grown in either sitting or hanging drops and appeared in 3−4 weeks. The antimycin A_1 (from *Streptomyces sp.* by Sigma) or NQNO (Sigma) bound bc_1 crystals were grown under similar conditions except that a 5-fold molar excess of antimycin A_1 or NQNO was added to the protein solution prior to crystallization. Both native and inhibitor bound bc_1 crystals had a rectangular shape ranging in sizes from 0.4 to 0.7 mm and were cryo-protected at a glycerol concentration of 30−40%. The inhibitor bound crystals were isomorphic to native crystals (Table 1). Partially reduced bc_1 crystals were grown under anaerobic conditions under Ar gas.

X-ray Diffraction Data Collection and Reduction. Crystals were stable at synchrotron radiation sources when cryo-cooled to 100 K, allowing collection of complete data sets during several hours of X-ray exposure. Data used in this study were collected on an ADSC CCD detector at the beamline X9B of the National Synchrotron Light Source (NSLS) of the Brookhaven National Laboratory (BNL), with a wavelength of 1.0 Å for the native and for the antimycin A_1 bound crystals. The NQNO data sets were collected on a MarCCD detector with a wavelength of 1.2 Å at the IMCA beamline, Advanced Photon Source (APS), Argonne National Lab (ANL). Raw diffraction frames were processed with DENZO, and integrated intensities were merged and scaled with SCALEPACK; both programs are part of the HKL package (*21*). Statistics for the quality of the diffraction data sets are provided in Table 1.

Data Analysis, Structure Refinement and Modeling. Programs from the CCP4 package (*22*) were used for merging and scaling different data sets, calculating structure factors from atomic models, performing density modifications, and computing Fourier maps. Structure refinements for the native and inhibitor bound crystals were carried out with the program REFMAC (*23*), using the atomic coordinates of the 2.2 Å resolution bc_1 structure (*9*) as a phasing model followed by iterative maximum likelihood positional and TLS (translation, libration, and screw tensor) refinement against respective diffraction data sets. The coordinates of antimycin A_1 (*12*) and NQNO (unpublished result) were obtained crystallographically, and the models were fitted initially into isomorphous difference electron density maps calculated between the respective complex and the native data set and subsequently refined. Omit maps were calculated with refined phases obtained by omitting either bound ligand or associated water molecules from the coordinates followed by maximum likelihood positional and TLS refinement. Between REFMAC refinement cycles, σ_A weighted $2mF_o-DF_c$, mF_o-DF_c, and F^+-F^- maps were calculated (*24*) and used for model corrections, identifying new structural features and solvent molecules in the program O (*25*). Statistics on qualities, completeness, and number of assigned solvent molecules of the refined bc_1 models is given in Table 1. Molscript (*26*), Bobscript (*27*), and Povray (www.povray.com) interfaced with GL-render (Esser, L., unpublished results) were used for atomic modeling and the molecular graphics presentation.

RESULTS

Structural Environment of the Q_i Site. The cyt. *b* subunit of the bovine bc_1 has 379 amino acid residues, consisting of eight membrane-spanning helices named sequentially from A to H with both the N- and the C-terminus located in the mitochondrial matrix (Figure 1). The eight helices are arranged in two helical bundles, one consisting of helices A−E and the other of helices F−H (*10*). The b_L and b_H hemes are incorporated into the first helical bundle and liganded by conserved histidine residues (His^{83} and His^{182} for the b_L, His^{97} and His^{196} for the b_H). Among the seven extra-membrane loops that link pairs of TM helices, four are prominent: they are the AB, CD, DE, and EF loops with the DE loop being the only one on the matrix side. These large loops are perhaps most important to the function of cyt. *b* as they are the primary participants in the formation of the Q_o and Q_i site. The AB and EF loop each contain one helix, namely, ab and ef; the CD loop has two helices, cd1 and cd2, in a hairpin arrangement; and the DE loop has no secondary structure element. While making contacts at the matrix side of the membrane, the two helical bundles separate from each other near the intermembrane space side of the membrane, thus creating the so-called Q_o pocket between the b_L heme and the 2Fe−2S cluster of ISP (Figure 1).

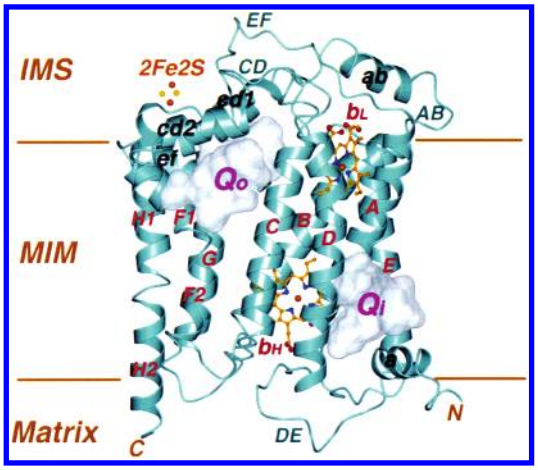

FIGURE 1: Ribbon presentation of the cyt. *b* subunit of bc_1. The subunit is oriented with the matrix side at the bottom of the page and the intermembrane space (IMS) on the top. The mitochondrial inner membrane (MIM) is roughly delineated with the two parallel lines in brown. The eight TM helices are labeled A−H. Four prominent surface loops are labeled as AB, CD, DE, and EF. The helices within the surface loops are labeled as ab, cd1, cd2, and ef. The two substrate binding pockets, Q_o and Q_i, are defined by cavity maps (*49*), portrayed in GRASP surfaces (*50*), and as labeled. The two intercalating hemes, b_L and b_H, are rendered as the ball-and-stick models with carbon atoms in yellow, nitrogen in blue, oxygen in red, and iron in orange. The 2Fe−2S cluster from subunit ISP is shown as balls with sulfur in yellow and iron in orange. All ribbon diagrams are produced with Molscript (*26*), Bobscript (*27*), and Povray (www.povray.com) interfaced with Gl-render (Esser, unpublished work).

The Q_i pocket is located near the matrix side of the membrane with its entrance open to the center of the membrane bilayer. From the entrance, the cavity dives nearly vertically toward the matrix side of the membrane and is surrounded by residues from transmembrane helices A (Trp^{31}, Asn^{32}, Gly^{34}, Ser^{35}), D (Ala^{193}, Met^{194}, Leu^{197}, His^{201}), and E (Tyr^{224}, Lys^{227}, Asp^{228}); the amphipathic surface helix a (Phe^{18}); the A loop (Ile^{27}); the DE loop (Ser^{205}, Phe^{220}); and atoms from the high-potential heme b_H (CMB, CMA, and one of the propionate side chains). These residues are identified by their interactions with the bound antimycin A_1 (Figure 2A), NQNO (Fgiure 2B), and substrate ubiqinone

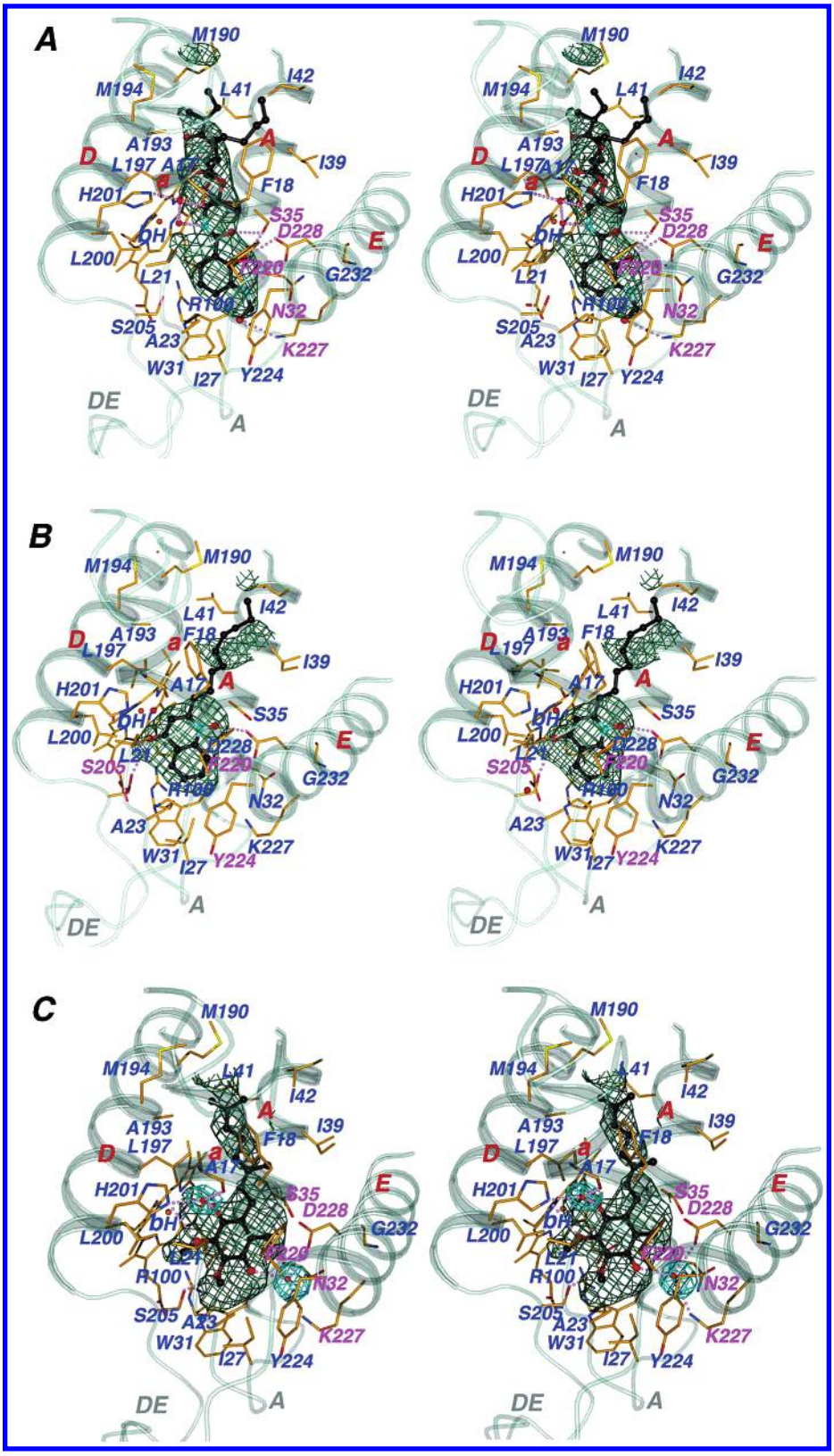

FIGURE 2: Stereopairs: interactions of the protein environment at the Q_i site of the cyt. *b* subunit with bound inhibitors and substrate. Secondary structure elements surrounding the Q_i pocket, including portions of the N-terminal helix a, TM helices A, D, and E, and extramembrane loops A and DE, are shown and are labeled. Residues interacting with bound inhibitors or substrate and the b_H heme are drawn in stick models and are labeled with carbon atoms in yellow, nitrogen in blue, oxygen in red, and iron in orange. H-bonds are indicated with the pinkish dotted lines. Water molecules are shown as the isolated red balls. The residues that are labeled magenta confer inhibitor resistance. Inhibitors and the substrate ubiquinone, caged in F_o-F_c electron densities calculated with refined phases after ligand being omitted and contoured at the 3σ level in dark green, are drawn as the ball-and-stick models with carbon atoms in black, nitrogen in light blue, and oxygen in red. (A) Q_i pocket with the bound antimycin A_1, (B) Q_i pocket with the bound NQNO, and (C) Q_i pocket with the bound ubiquinone with two isoprenoid units visible in electron density. Additionally, the two bound water molecules are enclosed in the F_o-F_c electron density in cyan calculated with refined phases obtained with the waters omitted and contoured at 3σ.

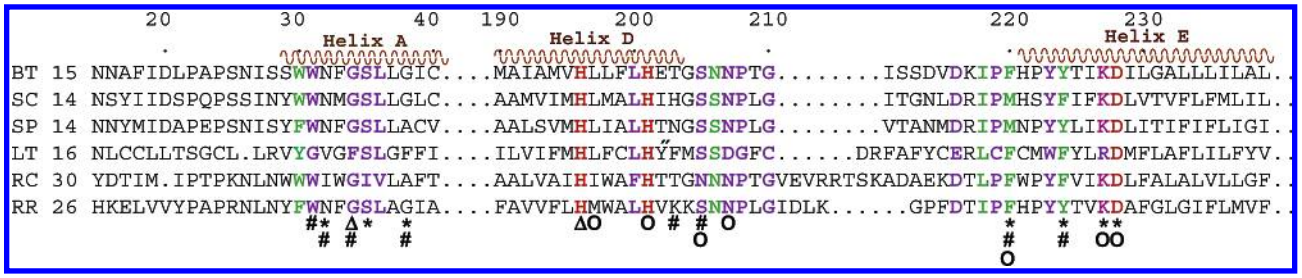

FIGURE 3: Sequence alignments of Q_i pocket residues of cyt. *b* subunits from different species: BT (*B. taurus*), SC (*S. cerevisiae*), SP (*S. pombe*), LT (*L. tarentolae*), RC (*R. capsulatus*), and RR (*R. rubrum*). The helical secondary structure elements are indicated with the sinuous curves in brown and as labeled. Amino acid positions in the bovine sequence are numbered above the sequences. Absolutely conserved residues in all sequences are colored red, those with a single conserved change are in magenta, and those with two or more conserved changes are in green. Underneath the sequences, the * indicates mutations at this position causing antimycin A resistance, the △ affecting cyt. *b* assembly, the # rendering NQNO resistance, and the ○ either abolishing or slowing down b_H heme reoxidation.

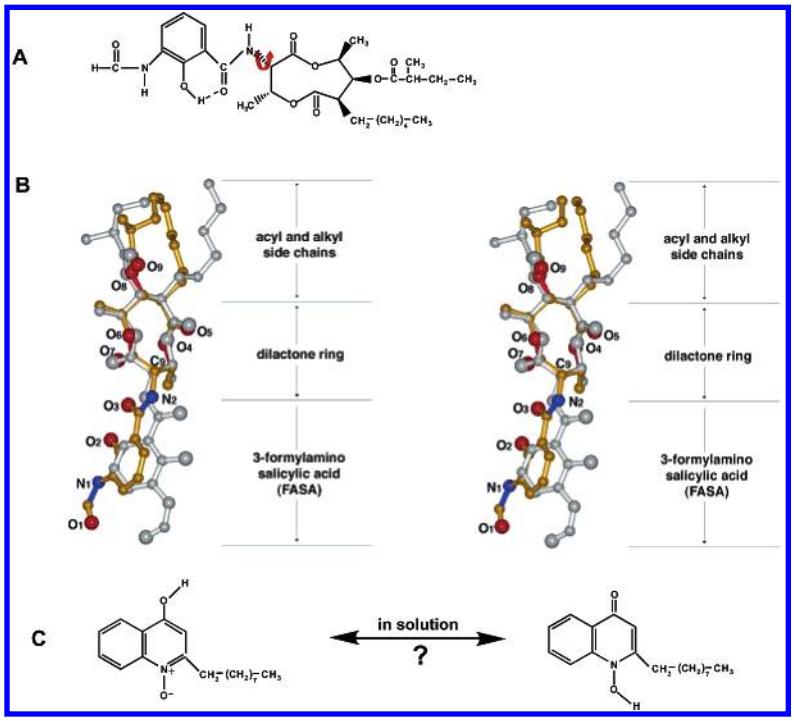

FIGURE 4: Structures of antimycin A_1 and NQNO. (A) Chemical structure of antimycin A_1. The flexible dihedral angle is indicated with a red curving arrow. (B) Stereopair: the superposition of the structures of antimycin A_1 in solid state (gray) and in complex with bc_1 (colored with carbon atoms in yellow, oxygen in red, and nitrogen in blue). The two structures are superimposed onto their respective dilactone rings. The three components of the molecule are as indicated; important oxygen and nitrogen atoms are as labeled. (C) Possible hydrogen configurations of NQNO in solution. The chemical structures of NQNO tautomers are shown. The hydrogen atom bound to the hydroxyl oxygen is proposed to equilibrate with that to the *N*-oxide oxygen in solution. In solid state, the hydrogen atom is shown to be attached to the *N*-oxide oxygen exclusively.

(Figure 2C) in the cyt. *b* subunit. Among these residues, Ser^{35}, His^{201}, Lys^{227}, Asp^{228}, and Ser^{205} are highly conserved (Figure 3) and located near the bottom of the pocket. The Q_i pocket has a hydrophobic entrance but turns progressively hydrophilic inward; it has the dimensions of roughly 7 × 10 × 13 Å and is potentially capable of accessing the mitochondrial matrix through the conserved residues His^{201} and Lys^{227} (see Discussion).

Binding Interaction of Antimycin A_1 with Cyt. b. The isomorphous difference electron density map calculated with Fourier coefficients between the antimycin A_1 bound and native bc_1 crystal showed a strong, well-defined peak in the Q_i pocket over 10σ above the mean and with the characteristic shape of antimycin A_1. Antimycin A_1 consists of three parts (Figure 4A,B): a nine-member puckered dilactone ring in the middle, a 3-formylamino salicylic acid (3-FASA) group that connects to the dilactone ring through an amide bond, and a hydrophobic tail on the other side of the dilactone ring comprised of a hexyl and a 1-methyl butanoate chain. In the complex with bc_1, antimycin A_1 penetrates deep into the Q_i pocket with the 3-FASA group making a network of six H-bonds and one Ar−Ar interaction (Figure 2A). Atoms OD1 and OD2 of Asp^{228} are 3.0 and 2.2 Å from the amide N1 and 3-FASA hydroxyl oxygen of the antimycin A_1, respectively. Atom OG of Ser^{35} is 2.6 and 2.9 Å, respectively, from the carbonyl oxygens O3 and O7 of the dilactone ring. Two water molecules, 2.8 Å apart and stabilized by the NE2 atom of the His^{201} (2.6 Å) and carbonyl oxygen of Ala^{17} (2.3 Å), respectively, each form a H-bond with atom N2 of the salicyl amide group (2.4 and 3.7 Å, respectively). Lys^{227} is 3.4 Å from the terminal carbonyl oxygen of the 3-FASA group. Phe^{220} has an edge-to-face distance to the 3-FASA ring of 3.1 Å, forming an Ar−Ar pair (*9*). One of the b_H heme's propionates curves away from the heme porphyrin

plane, forming an ion pair with the Arg^{100} and whose hydrophobic side chain stabilizes the 3-FASA by van der Waals interactions (Figure 2A). Additionally, there are a number of van der Waals contacts between the bound antimycin A_1 and its protein environment: deep inside the pocket the residues Ile^{27}, Trp^{31}, Asn^{32}, and Phe^{224} are in contact with the formyl group of the 3-FASA; at the entrance of the Q_i pocket, the dilactone ring makes contacts with Phe^{28}, Gly^{38}, Leu^{197}, and the b_H heme. The 1-methyl butanoate tail is near the entrance of the Q_i pocket in contact with Met^{194} and Met^{190}, whereas the disordered hexyl tail remains outside the Q_i pocket with no contact with the cyt. *b* subunit.

Binding Interaction of NQNO with Cyt. b. Isomorphous difference electron density calculated with Fourier coefficients of $F_o^{NQNO}-F_c^{nat}$, where F_o^{NQNO} and F_c^{nat} are the structure factor amplitudes for the NQNO bound and for the calculated native bc_1 crystal, respectively, showed a flat triangular shaped electron density at the Q_i pocket inserted in the space between residues Asp^{228} and His^{201}. The NQNO molecule was best modeled into the density with the *N*-oxide oxygen near the carboxylate group of Asp^{228} and the hydroxyl group close to the His^{201}. The hydrophobic tail of NQNO except for the first two carbon atoms was not visible (Figure 2B). Two residues are in H-bonding distance from the inhibitor: the carboxylate group of Asp^{228} is 2.9 Å from the *N*-oxide of NQNO; the OG of Ser^{205} is 3.2 Å from the hydroxyl group of NQNO. The imidazole ring of His^{201} is not in the right orientation to form H-bonds with the bound inhibitor despite close proximity. The edge of the phenyl ring of Phe^{220} is 3 Å from the center of the quinoline ring of NQNO, ideal for an Ar−Ar interaction (*9*). Additional interactions are contributed by residues in van der Waals distances from the heme b_H, Phe^{18}, Ser^{35}, Leu^{197}, Leu^{200}, and Tyr^{224}.

Binding Interaction of Ubiquinone with Cyt. b. The ubiquinone molecule identified in the native bc_1 crystal was copurified and cocrystallized, which diffracted X-rays to 2.6 Å resolution (Table 1). In the refined structure, a piece of electron density was located at the Q_i site of the cyt. *b* subunit more than 5σ above the mean, into which a ubiquinone molecule with its first two isoprenoid repeats was fitted. The two possible orientations of the planar ubiquinone ring could not be distinguished from the shape of the electron density, and refinements with both orientations gave identical statistics (Figure 2C). The orientation of the ubiquinone adopted here is based on continuity of electron density at a higher σ cutoff and consideration to the quinone reduction mechanism (see Discussion). The average *B* factor of the bound ubiquinone is twice as large as its immediate protein environment, suggesting a lower than 50% occupancy in the crystal. The quinone ring is nearly perpendicular to the plane of the phenyl ring of Phe^{220} and to that of heme b_H; the former forms an Ar−Ar pair with the ubiquinone (3.0 Å), and the latter has the closest distance of 4.2 Å (Figure 2C). There are three H-bonds formed between the bound ubiquinone and the Q_i site residues: the OD2 of Asp^{228} is 2.3 Å away from a structural water molecule, to which one of the carbonyl oxygens O14 of the ubiquinone connects with a distance of 2.6 Å; the NE2 of His^{201} interacts with the other carbonyl oxygen O11 of the ubiquinone via another structural water molecule with distances of 2.2 and 2.6 Å, respectively. The existence of these water molecules was confirmed with omit map calculation, and their roles will be discussed in connection to the mechanism of ubiquinone protonation reactions (see Discussion). The O13 of the methoxy group is 2.8 Å from the OG of Ser^{205}. The two isoprenoid repeats that were visible in the electron density are in contact with residues Phe^{18}, Ser^{35}, Gly^{38}, Met^{190}, Leu^{197}, and the b_H heme.

Binding of NQNO to the Q_o Pocket. A piece of electron density in the isomorphous difference map calculated with Fourier coefficients of $F_o^{NQNO}-F_c^{nat}$, 5σ in height and triangular in shape, appeared at the Q_o site and was intercalated between the cd1 helix and the conserved PEWYF sequence in the EF loop just before the ef helix (Figure 5). Specific interactions of the bound inhibitor with residues lining the wall of the Q_o pocket include a water-mediated H-bond with distances of 3.5 and 3.0 Å from the *N*-oxide of NQNO and the OE of Glu^{271}, respectively, to the water molecule; and the hydroxyl group of NQNO 3.5 Å to the NE2 of the His^{161} imidazole ring, which is one of the four ligands to the 2Fe−2S cluster of ISP. The following residues are in van der Waals distances from the NQNO: Met^{138}, Gly^{142}, Leu^{145}, Ile^{146}, Pro^{270}, and Phe^{274}.

Conformational Changes in Cyt. b upon Binding of Inhibitors at the Q_i Site. Antimycin A_1 is conformationally rigid with practically only one flexible dihedral angle bridging the 3-FASA group and the dilactone ring between the atoms C9 and N2 (Figure 4A,B). Superposition of the dilactone ring of the free antimycin A_1 in the crystalline state with that bound in the bc_1 complex showed a nearly 180° rotation of the 3-FASA moiety around this dihedral axis, thus gaining at least four H-bonds with the protein environment in the inhibitor complex. The nine-membered dilactone ring has limited flexibility and displays slightly different puckering when bound to the Q_i pocket. Structure alignment between the native and the inhibitor bound cyt. *b* subunits produced an rmsd of 0.33 Å for 377 out of 379 Cα atoms, suggesting an overall structural rigidity of the cyt. *b* subunit. Among the antimycin A interacting residues, four undergo significant conformational changes when antimycin A_1 binds (Figure 6A): the hydroxyl group of Ser^{35} flipped nearly 100° around $\chi1$ forming two H-bonds with the bound antimycin A_1; the imidazole ring of His^{201} is rotated 110° around $\chi2$; the phenyl group of Phe^{18} is rotated 90° around $\chi1$ moving away for inhibitor entry; and the terminal methyl group of Met^{194} is rotated to accommodate the dilactone moiety of the antimycin A_1. The heme b_H, Phe^{220}, and Asp^{228} have no detectable conformational changes between the native and the inhibitor bound cyt. *b*. The antimycin A_1 molecule apparently binds slightly deeper into the Q_i pocket and interacts with residues (Ser^{35} and Asp^{228}) located on the same side of the pocket. Interestingly, in the complex the hydroxyl group in the 3-FASA ring of antimycin A_1 occupies almost the identical position as the methyl group of the bound ubiquinone in the substrate complex (Figure 6A); likewise, the water molecule that H-bonds to the amide nitrogen (N2) in the antimycin complex occupies a nearly identical position as the carbonyl oxygen O14 of the bound ubiquinone in the substrate complex. Binding of antimycin A_1 does not alter the anomalous signals of the iron atoms for b_L, b_H, c_1, and 2Fe−2S (Table 2).

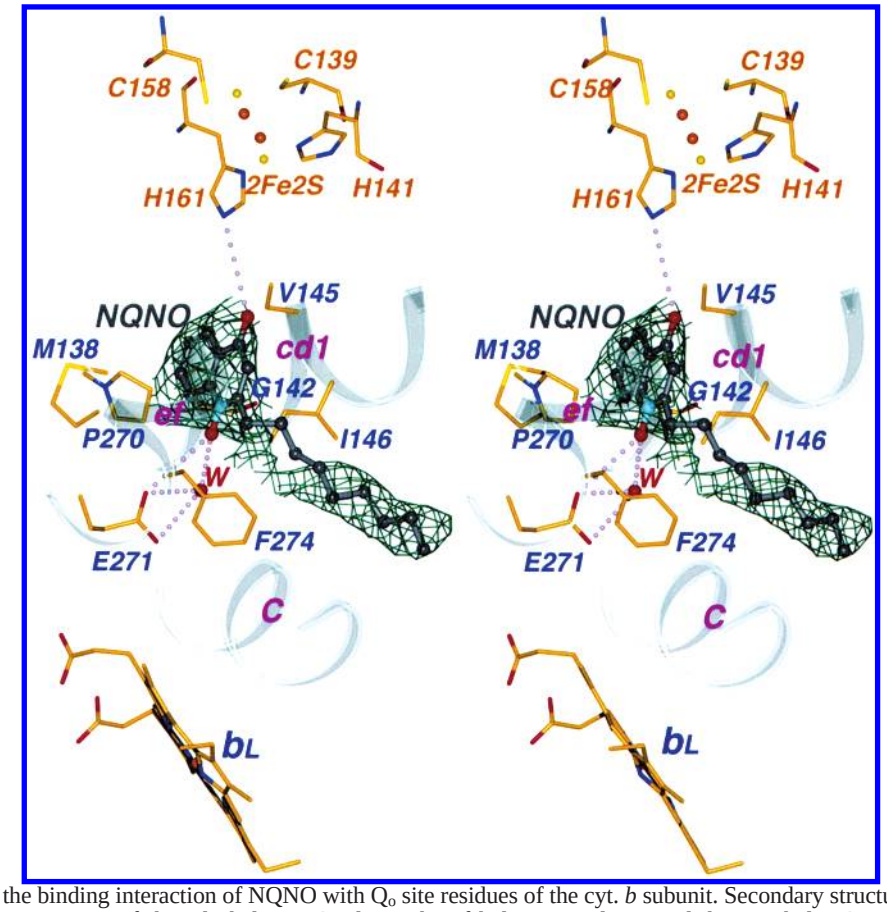

FIGURE 5: Stereopair: the binding interaction of NQNO with Q_o site residues of the cyt. *b* subunit. Secondary structure elements surrounding the Q_o pocket, including portions of the cd1 helix in CD loop, the ef helix in EF loop, and the TM helix C are shown and as labeled. Residues that are interacting with the bound NQNO and the b_L heme are drawn as the stick models with carbon atoms in yellow, nitrogen in blue, oxygen in red, and iron in orange and as labeled. H-bonds are indicated with the pinkish dotted lines. Water molecules are shown as the isolated red balls. The NQNO is caged in the $2F_o-F_c$ electron density contoured at 1.0σ level in dark green and drawn as the ball-and-stick model with carbon atoms in black, nitrogen in light blue, and oxygen in red. The ball-and-stick models of the four 2Fe−2S ligands of ISP are also shown.

Table 2: Normalized Anomalous Peak Heights for Iron Atoms in Various bc_1 Crystals

	normalized anomalous peak heights[a]			
	b_H	b_L	c_1	2Fe−2S
native	1.0	0.753	0.537	0.517
ubiquinone	1.0	0.843	0.537	0.244
antimycin A_1	1.0	0.892	0.566	0.312
NQNO1	1.0	0.770	0.433	0.832
NQNO2	1.0	0.702	0.501	0.646
variances[b]	0.0000	0.0047	0.0020	0.0464

[a] The two native and the one antimycin A_1 data sets were collected at a wavelength of 1.0 Å, and both NQNO data sets were collected at a wavelength of 1.2 Å. All anomalous difference maps were calculated with reflections in the resolution range between 40 and 4.5 Å. [b] Variances is defined as $[\sum(x_i - \langle x\rangle)^2]/N$, where $\langle x\rangle$ is the mean peak height.

Superposition of cyt. *b* subunits between the native and the NQNO bound gave rise to a rmsd of 0.40 Å for 378 residues. The *N*-hydroxy pyridone ring of the bound NQNO largely overlaps with the ubiquinone ring found in the substrate complex, and the two ring planes are slightly off by <5° (Figure 6B). Conformational changes observed for the Q_i site residues as a result of the NQNO binding are very limited when compared to the native bc_1 with bound ubiquinone. Large changes include that the $\chi 1$ angle of Asp^{228} is rotated by more than 30° and the position of the His^{201} residue is moved by nearly 1 Å.

Conformational Changes Near the Q_o Pocket upon NQNO Binding. The rmsd from the alignment of cyt. *b* subunits between the native and the NQNO bound (0.40 Å) was larger than that between the native and the antimycin A_1 (0.33 Å), even though conformational variations around the Q_i site appeared minimal. However, large conformational changes were observed for residues in the Q_o pocket when NQNO was bound (Figure 6C). The cd1 helix and part of the EF loop including the conserved PEWY sequence underwent significant displacement in opposite directions, opening up a seam in the Q_o pocket and letting the NQNO headgroup sneak in to form an H-bond with the His^{161} of ISP. The side chain of Glu^{271} swung 180° around the dihedral angle $\chi 1$ to form an H-bond with the *N*-oxide oxygen of the bound NQNO via a structural water molecule. Observed conformational changes in the inhibitor complex upon NQNO binding were not limited locally to the residues interacting with the inhibitor. Conformational arrest of the ISP induced by NQNO binding was observed in both diffraction data sets we collected (Table 2). Top peaks representing iron atoms in the bc_1 crystals in anomalous difference maps were calculated for the native with and without substrate, with bound antimycin A_1, and with NQNO; peak heights were normalized to that of the b_H heme iron, and the variance for each type of iron was given. Clearly, binding of NQNO forced the ISP subunit to undergo a binary conformational switch from a loose to a fixed state.

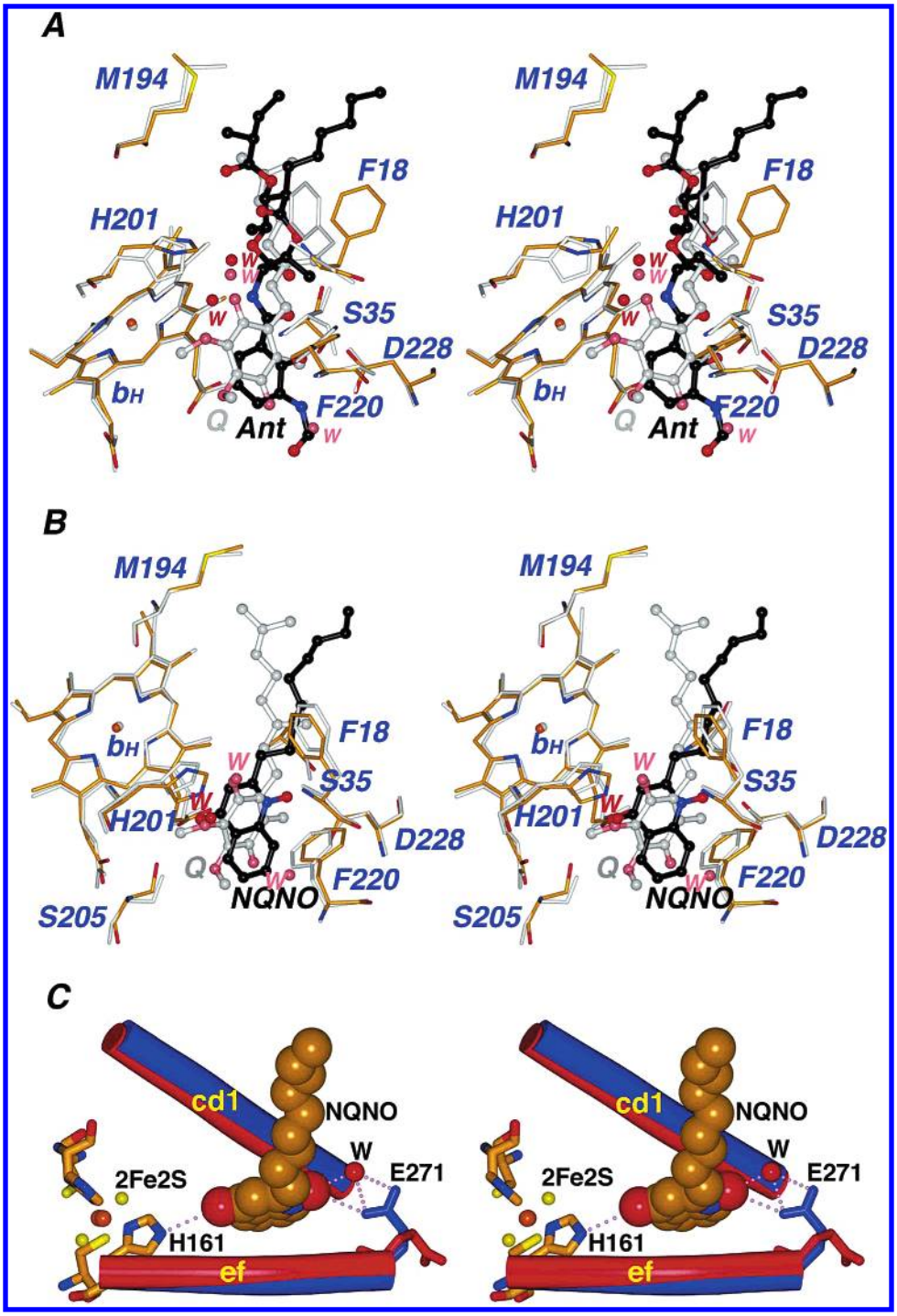

FIGURE 6: Stereopairs: conformational variations at the inhibitor binding pockets. (A) Antimycin A_1 bound vs native bc_1 at the Q_i pocket. The antimycin A_1 in the complex is shown as the ball-and-stick model with carbon atoms in black, oxygen in red, and nitrogen in blue; the surrounding residues and the heme b_H are drawn as the stick models with the same color scheme except for the carbon atoms that are in yellow and are as labeled. The bound ubiquinone, its surrounding residues, and the b_H heme in the native structure are shown as the ball-and-stick models in gray. The water molecules in the antimycin A_1 bound and in native structure are shown as the isolated balls and colored in red and magenta, respectively. (B) NQNO bound vs native bc_1 at the Q_i pocket. The NQNO and its surrounding residues in the complex are shown as the ball-and-stick model and as labeled; the color scheme is the same as in panel A. The bound ubiquinone and its contacting residues in the native structure are also shown as the ball-and-stick models in gray. (C) NQNO bound vs native bc_1 at the Q_o pocket. The bound NQNO is shown as the CPK model with the carbon atoms in yellow, nitrogen in blue, and oxygen in red. The cd1 and ef helices are drawn as cylinders colored in red for the native and blue for the inhibitor complex. Residues in the cyt. *b* subunit that undergo large conformational changes upon NQNO binding are also shown. The 2Fe−2S cluster of ISP together with its ligands are also depicted and as labeled.

DISCUSSION

Structural Basis of High Affinity Binding of Antimycin A. Among specific inhibitors of bc_1 complexes, antimycin A has the highest binding affinity (*6*), which is reflected by its low thermal motion observed crystallographically. The mean *B* values for the bound antimycin A are 36.8 and 41.6 $Å^2$, respectively, for the 26 ordered atoms and for the entire

molecule (39 atoms). As a comparison, the mean *B* value for the cytochrome *b* subunit is 34.6 Å^2, consistent with high affinity binding of antimycin A. The use of various chemically modified antimycin A derivatives identified the following important structural features: first, among the five chiral centers in the dilactone ring, the S configuration for atom C9, through which the 3-FASA group is attached, rendered it 100-fold more potent (*28*). Second, the shape of antimycin A is strictly recognized by the Q_i pocket; the salicylic acid moiety appeared to be more important than the dilactone ring for binding (*29*, *30*). An intramolecular H-bond between the phenolic OH (O2) and the carbonyl oxygen (O3) of the benzamide group is required to maintain the conformational integrity of antimycin A for inhibition; a 10 000-fold reduction in binding affinity was observed as a result of disruption of this H-bonding (*31*). Third, N-methylation of the benzamide was shown to dramatically reduce binding affinity (1000-fold) (*31*). Finally, N-methylation of the terminal formylamino group showed a reduction of binding affinity by 164-fold (*31*). Prior structural studies of bc_1 in complex with antimycin A_1 (*8*, *10*−*12*) identified the approximate location and orientation of the bound inhibitor in the cyt. *b* subunit but failed to adequately address the origin of antimycin A binding affinity. The available coordinates of antimycin A in complex with chicken bc_1 (PDB 3BCC) showed two strong H-bonds between the 3-FASA moiety and Glu^{229} (2.4 and 2.8 Å) and a weak H-bond (3.6 Å) between the terminal formyl oxygen and Lys^{228}, which is not consistent with extensive literature and the extraordinarily high binding constant. In our study, the initial model for bc_1 was obtained from the 2.4 Å structure (*9*) and that for antimycin A_1 was from the crystal structure (*12*); both the native and the antimycin A_1 bound bc_1 were refined to 2.4 and 2.6 Å resolution, respectively (Table 1). We consider that the structures of the cyt. *b* subunit of this work are more reliable. Unlike the severely distorted inhibitor molecule in the structure of 3BCC, the antimycin A_1 molecule in our study maintains a rigid shape with only one variable dihedral angle connecting the dilactone and 3-FASA moiety (Figure 4B). The intramolecular H-bond between the phenolic OH and the carbonyl oxygen of the benzamide is maintained; as a result, the 3-FASA moiety is planar. The formylamino group is maintained coplanar with the rest of the 3-FASA group. In the complex, five strong H-bonds (distances <3 Å) and one weaker H-bond (distance <3.5 Å) are available for binding interactions in addition to one pair of Ar−Ar interactions (Figure 2A), consistent with experimentally observed high binding affinity of antimycin A. Furthermore, both amide nitrogen atoms are involved in the H-bonding interaction, in line with the fact that N-methylations at these groups severely reduced the antimycin A binding affinity.

NQNO Is a Dual Site bc_1 Inhibitor. Most bc_1 inhibitors bind to either the Q_i or the Q_o site but not both; it appears that binding of an inhibitor to one site with high affinity makes it less likely to be a specific inhibitor of the other. A conceivable reason appears to be in the differences in geometry and binding environment between the two pockets; it implies that the substrate ubiquinol/ubiquinone, capable of accepting and delivering electrons at the Q_i and Q_o site, respectively, should not be a good binder at either site, which is indeed the case crystallographically. NQNO mimics the structure of the quinone/quinol molecule in such a way that renders it capable of binding to both Q_i and Q_o sites but at the cost of a relatively low binding affinity to either site. Unlike substrate quinone/quinol that can be either all protonated or deprotonated, NQNO maintains one protonated (-OH) and one deprotonated (-NO) group (Figure 4C). With this configuration, only one H-bond forms between the hydroxyl group of the inhibitor and the OG atom of Ser^{205} in the Q_i site. The *N*-oxide group of NQNO, although close to Asp^{228}, does not provide specific interaction. On the basis of crystallographic and NMR studies of the solid-state NQNO (data not shown, this paper) as well as similar compounds in the literature (*32*), the hydrogen atom is attached to the *N*-oxide oxygen rather than to the carbonyl oxygen. However, it is possible that in solution the hydrogen atom associated with the hydroxyl group of NQNO can be in equilibration between the two positions (i.e., the hydroxyl and the *N*-oxide oxygen (Figure 4C)). This alternative configuration (tautomers) would allow an additional H-bond to be formed between the N−OH of NQNO and Asp^{228}. Similarly at the Q_o site, when the hydrogen atom is associated with the *N*-oxide group, two H-bonds would be formed between the inhibitor and the Q_o site residues. To confirm experimentally the association of the hydrogen atom with the *N*-oxide of NQNO in the complex, high-resolution X-ray diffraction data or a neutron diffraction experiment would be necessary.

NQNO was known to be a Q_i site inhibitor; its effect to the Q_o site reaction was suggested but never clearly established (*14*). The crystallographic data demonstrated that NQNO is capable of binding to both Q_i and Q_o sites and is therefore a better quinone analogue. As a Q_o inhibitor, NQNO behaves most similarly to stigmatellin in its ability to reduce the ISP mobility (Table 2), to form two characteristic H-bonds: one with His^{161} of ISP and the other with Glu^{271}, and to cause identical conformational changes to the side chain of Glu^{271}.

Mechanism of Resistance for Q_i Site Inhibitors. Antimycin A resistance mutations in the bc_1 complex from various species were reported; when mapped onto the atomic model of cyt. *b* with bound antimycin A, all of them were located in the immediate vicinity of the inhibitor binding pocket (Table 3, Figure 2A) (*33*−*38*). Mutations 1 and 2 in Table 3 each cause the loss of two strong H-bonding interactions important to inhibitor binding. Mutations 3 and 4 would not only block the inhibitor from entering the Q_i site but also hinder the entry of the substrate ubiquinone into the O_i pocket. Indeed, these mutations also display altered kinetics of quinone reduction (*3*). Both Glu^{228} and Lys^{227} are important for H-bonding to antimycin A and are 3.3 and 3.7 Å away from Asn^{32}; equivalent mutation N31K in yeast (mutation 5 in Table 3) would disrupt the delicate charge balance at the site between Glu^{228} and Lys^{227} resulting in changes in available H-bonding donors and acceptors as well as in the shape of the Q_i pocket. Phe^{220}, conserved in most species but not in yeast, forms an Ar−Ar interaction with the bound ubiquinone and antimycin A_1, contributing to the binding affinity to both and perhaps holding the ubiquinone molecule in a proper orientation for the ET reaction (Figures 2C and 3). Mutations at this position in yeast M221E,Q (mutation 6 in Table 3) would severely modify the shape of the Q_i pocket, not only producing antimycin A resistance but also leading to a defective phenotype in ubiquinone

Table 3: Antimycin A Resistant Mutants and Possible Mechanism of Resistance

no.	residue change	species	bovine equivalent	possible mechanism of resistance	ref
1	S35I	*L. tarentolae*	S35	reduced $IC_{50} = 10-20$ ng/mL (wild-type $IC_{50} = 1$ ng/mL) by losing two H-bonds	*32*
2	D252A,N	*R. capsulatus*	D228	loss of two H-bonds with the carbonyl O7 of the dilactone group and the benzamide O3	*45*
	D243H,E	*R. rubrum*			*37*
3	A52V	*R. capsulatus*	G38	Cα is 3.8 Å to the C16 of the dilactone ring, blocking the entrance to the Q_i pocket	*3*
	G37V	*S. cerevisiae*			*34*
	A37V	*S. pombe*			*33*
	G38V	mouse			*36*
4	G232D	mouse	G231	blocks the entrance and limits antimycin A access to the Q_i site	*36*
5	N31K	*S. cerevisiae*	N32	is 3.5 Å away from Glu^{228} and potentially competes for Glu^{228} with antimycin A	*34*
6	M221E,Q	*S. cerevisiae*	F220	loses van der Waals contacts with the 3-FASA group of antimycin A	*35*
7	K251M,I	*R. capsulatus*	K227	loses one H-bond with the formyl O1 and interaction with bound lipid phosphates and	*45*
	K228I,M	*S. cerevisiae*		may collapse into the Q_i binding site	*34*

Table 4: HQNO (NQNO) Resistant Mutants and Possible Mechanism of Resistance

no.	residue change	species	bovine equivalent	possible mechanism of resistance	ref
1	W30C	*S. cerevisiae*	W31	is 5 Å from the bound NQNO and likely to change the shape of NQNO binding environment	*a*
2	N31K	*S. cerevisiae*	N32	is 3 Å from Asp^{228} and likely to change Asp^{228} interaction with NQNO	*3*
3	G33A	*S. cerevisiae*	G34	changes b_H heme packing orientation and alters NQNO binding environment	*38*
4	A52V	*R. sphaeroides*	G38	are likely to block the entrance of the Q_i pocket and affect Q_i kinetics	*50*
	G37V	*S. cerevisiae*	G38		*3*
5	H204Y	*S. cerevisiae*	T203	is in short distance from Ser^{205} and may disrupt Ser^{205} interaction with the bound NQNO	*37*
6	S206L	*S. cerevisiae*	S205	H-bond to the bound NQNO and the Q_i kinetics disturbed	*38*
	S206V	*S. cerevisiae*	S205		*49*
7	M221E	*S. cerevisiae*	F220	Lose proper interaction with NQNO and may fail to maintain the shape of the Q_i pocket	*38*
	M221Q	*S. cerevisiae*	F220		*38*
8	F225L	*S. cerevisiae*	Y224	is 3.5 Å from the bound NQNO and may alter the shape of Q_i pocket	*3*

[a] Brasseur, G. (1995) Ph.D. Thesis, University of Aix-Marseille I, France.

reduction (*39*). Lys^{227} is making an H-bond with the terminal formylamino group of the 3-FASA; the mutations K227M,I result in loss of the H-bonding. This mutation also leads to slow ubiquinone reduction since this residue in the cyt. *b* subunit with substrate bound helps to stabilize a water molecule (3.5 Å) that binds directly to the carbonyl oxygen of the bound ubiquinone (Figure 2C). Lys^{227} is also speculated to be a proton shuttle obtaining protons from the mitochondrial matrix (see following paragraphs and ref *17*). In essence, the common mechanism underlying antimycin A resistance is through inhibitor exclusion either by dramatically reduced binding affinity (mutations 1 and 2 in Table 3) or by modification of the binding pocket (mutations 3−5 in Table 3) or both (mutations 5−7 in Table 3).

Reported mutations that rendered NQNO or HQNO resistance are extensive; all are located in the immediate vicinity of the Q_i pocket. When compared with the antimycin A resistance mutations, it is clear that the set of NQNO resistance mutations does not entirely overlap with that for antimycin A, suggesting nonidentical binding sites. Consistent with the genetic data, crystallographic observations show that some of the residues in the Q_i pocket interacting with the bound antimycin A_1 do not contribute to NQNO binding and vice versa. For example, Ser^{35} forms two H-bonds with the bound antimycin A_1 but is over 4.6 Å away from the bound NQNO. Likewise, Ser^{205} H-bonds to NQNO but has a distance of 4 Å from antimycin A_1. Mutations that render resistance to NQNO are given in Table 4. Two types of inhibitory mechanisms can be conceived: (1) steric hindrances by mutations altering the size and morphology of the binding pocket, such as mutations 1, 3, 4, 7, and 8 in Table 4 and (2) perturbation of specific binding interactions to NQNO either directly or indirectly as mutations 2, 5, and 6 in Table 4. In particular, the two residues that provide specific H-bonding interaction to the bound NQNO in our crystallographic observations were targets for mutations that rendered resistance. S205L,V would eliminate one of the two H-bonds. Asn^{32} H-bonds to Asp^{228} that interacts directly to the bound NQNO (Figure 2B), and mutations N32K would result in charge imbalance and disruption of the H-bond of Asp^{228} to the bound NQNO.

Mechanism of ET Inhibition. Ubiquinone binding at the Q_i site involves three H-bonds to the three Q_i pocket residues Asp^{228}, His^{201} and Ser^{205}; the first two residues interact with the two carbonyl groups of the bound ubiquinone, respectively, mediated by two bound water molecules (Figure 2C). These highly conserved residues are also used for inhibitor binding forming specific H-bonds. Asp^{228} and His^{201} provide four H-bonds for antimycin A binding; Asp^{228} and Ser^{205} are used for NQNO binding. Therefore, one strategy for bc_1 inhibition would be to compete for binding to these residues. The 3-FASA group of antimycin A mimics the shape of and occupies an almost identical position of the ubiquinone ring in the Q_i pocket (Figure 6A). Instead of having one water-mediated H-bond with the substrate, Asp^{228} forms two strong H-bonds with the bound antimycin A_1; the H-bonding of ubiquinone with His^{201} is also preserved for antimycin A_1 via the same water molecule. Antimycin A acquires three additional H-bonds via Ser^{35} and Lys^{227}, whereas the bound ubiquinone has only one additional H-bond between one of the methoxy oxygens and Ser^{205}. By using analogous binding geometry and providing more specific interactions, antimycin A is able to compete with the substrate for binding.

NQNO, when compared with antimycin A, is a much weaker Q_i site inhibitor with two H-bonds and one Ar−Ar interaction, similar to the substrate binding, consistent with

the fact that NQNO inhibition of bc_1 was reversed by excess amount of substrate (*40*, *41*). Our crystallographic data demonstrated that the NQNO is a dual site inhibitor capable of binding to the Q_o pocket as well. The dual binding mode of NQNO illustrates yet another mechanism of bc_1 inhibition, suggesting that the effect of the combined binding affinity of NQNO to both the Q_i and Q_o sites could be additive, even though the inhibitor interacts weakly to either site.

Electron-Transfer Mechanism at the Q_i Site. A model of bound ubiquinone at the Q_i pocket was given in the PDB entry 1BCC, although no description was found in the related article (*11*). More recently, in the 2.3 Å resolution structure of yeast bc_1, a ubiquinone (UQ6) at the Q_i site was modeled and refined (*16*). Similar to what we found in the bovine bc_1, the bound UQ6 has an average *B* factor twice as large as those of surrounding residues, most likely indicating a low occupancy in the crystal. Furthermore, the authors acknowledged the possibility of alternative conformations for the bound ubiquinone and postulated an H-bonding network that includes a protonated Asp^{229} (Asp^{228} in bovine) for UQ6 binding and possible involvement of His^{202} (His^{201} in bovine) as a proton donor. We reason that, to provide a suitable environment for the ubiquinone reduction and protonation, the Q_i pocket must satisfy the following requirements: first, it should have higher affinity for ubiquinone than for ubiquinol. Second, it must have access to protons from the mitochondrial matrix. And finally, the protein environment must be able to stabilize the ubisemiquinone free radical (*42*−*44*).

Structure alignment between the cyt. *b* subunits with and without bound ubiquinone gave rise to an rmsd of 0.24 Å; no significant conformational rearrangement was detected for residues at the Q_i pocket upon substrate binding. The two highly conserved residues His^{201} and Asp^{228} are 9.8 Å apart, between which there are four water molecules forming a network of H-bonds. Apparently, binding of substrate ubiquinone would require displacement at least two or more of these water molecules. Structure superposition between cyt. *b* subunits of bovine and yeast bc_1 produced an rmsd of 0.73 Å for 376 out of 379 Cα pairs; the superimposed Q_i pocket with both ubiquinones is given in Figure 7A. Most residues lining the wall of the Q_i pocket are conserved between the two species except for the four: F18I, L21S, A23Q, and F220M, among which only the Phe^{220} is in direct contact with the bound substrate. In bovine, two water molecules each mediate an H-bond to the substrate from Asp^{228} and His^{201}, respectively, whereas only one water-mediated H-bond in the Q_i pocket was seen in the yeast between His^{202} and the bound quinone. Significant conformational differences of equivalent residues in the Q_i pockets between bovine and yeast are observed for two residues only, namely, the His^{201} and Lys^{227}. The two $\chi 1$ angles of His^{201} are roughly 90° away from each other with that of bovine being much closer to the bound ubiquinone (Figure 7A). Located near the bottom of the Q_i pocket and existing in two different conformations, the imidazole ring of His^{201} could be used to fetch protons from the matrix. Lys^{227} is located at the bottom of the Q_i pocket but on the opposite side of the His^{201} and can be modeled in two different conformations (Figure 7A). In one conformation, the terminal amine is <3.5 Å from the bound water molecule that interacts with both Asp^{228} and the substrate. In an alternative conformation, illustrated in Figure 7A and observed in all refined bovine bc_1 crystals, the amine atom is rotated nearly 180° to interact with Asp^{223} of cyt. c_1, forming a positively charged cluster that interacts with the head ground of a bound lipid (data not shown) at the membrane interface, which could potentially be used as a channel for retrieving protons from the matrix. When the Q_i pockets of bovine and yeast are aligned, the terminal NE atoms of Lys^{227} of the two species point to different directions (Figure 7A). A similar observation was made in the yeast structure by Lange et al. (*17*) for the Lys^{228} (Lys^{227} in bovine) that was proposed to form one of the two possible proton uptake pathways.

Like that in the yeast structure, the ubiquinone in the bovine complex has an average *B* factor twice as large as those of the surrounding residues and could be modeled in two different ways without affecting the refinement statistics. One possible model has the headgroup of the ubiquinone in a similar orientation to that of yeast, whereas the other, giving rise to better electron density, flips the headgroup by 180°. Both models accommodate the two bound water molecules and therefore will not affect the outcome of the quinone reduction and protonation mechanism discussed below. However, it is possible that both ubiquinone conformations observed at the Q_i site exist, as those described for the ubiquinone molecules at the Q_B site in the photosynthetic reaction center of *Rhodobacter sphaeroides*, where the headgroup of bound ubiquinone underwent a 180° flip and the entire molecule moved by as much as 4.5 Å as the complex experiencing the transition from the dark to light condition (*45*).

In the sequence alignment of Q_i site residues (Figure 3), His^{201}, Lys^{227}, and Asp^{228} are highly conserved. His^{201} binds to the carbonyl oxygen of the bound ubiquinone through a water molecule; Asp^{228} interacts with the other carbonyl oxygen via another water molecule that was stabilized by Lys^{227} (Figure 2C). Mutations of His^{201} and Asp^{228} led to a defective phenotype in heme b_H reoxidation, suggesting that ET from b_H to ubiquinone was blocked (*46*). Mutations of Lys^{227} were not lethal but significantly reduced the rate of quinone reduction. These studies demonstrated the critical importance of these three Q_i pocket residues.

On the basis of available structural, phylogenetic, and mutational information, we propose a two-water molecule-mediated four-step mechanism for quinone reduction and protonation at the Q_i site, which is schematically illustrated in Figure 7B. The structure of native bc_1 without bound substrate is considered step I in Figure 7B, where the residues Asp^{228}, His^{201}, Ser^{205}, and Lys^{227} are poised to receive a ubiquinone molecule. When a ubiquinone molecule diffuses into the Q_i pocket, it is stabilized by three H-bonds; two of them are water mediated, which are critical in providing protons for the reduced ubiquinol. This is illustrated in step II of Figure 7B and represented by the bc_1 structure in the presence of ubiquinone. Asp^{228} is deprotonated whereas Lys^{227} is protonated, each making an H-bond to a bound water molecule that is also in H-bonding distance to the carbonyl oxygen of the ubiquinone. The His^{201} is also deprotonated and makes an H-bond with the water molecule that interacts with the other carbonyl oxygen of the ubiquinone. Hydrogen bonds to both carbonyl groups of quinone would elevate the midpoint potential of the bound Q ($Q^{\bullet -}$/Q) sufficiently high to accept the first electron from the heme

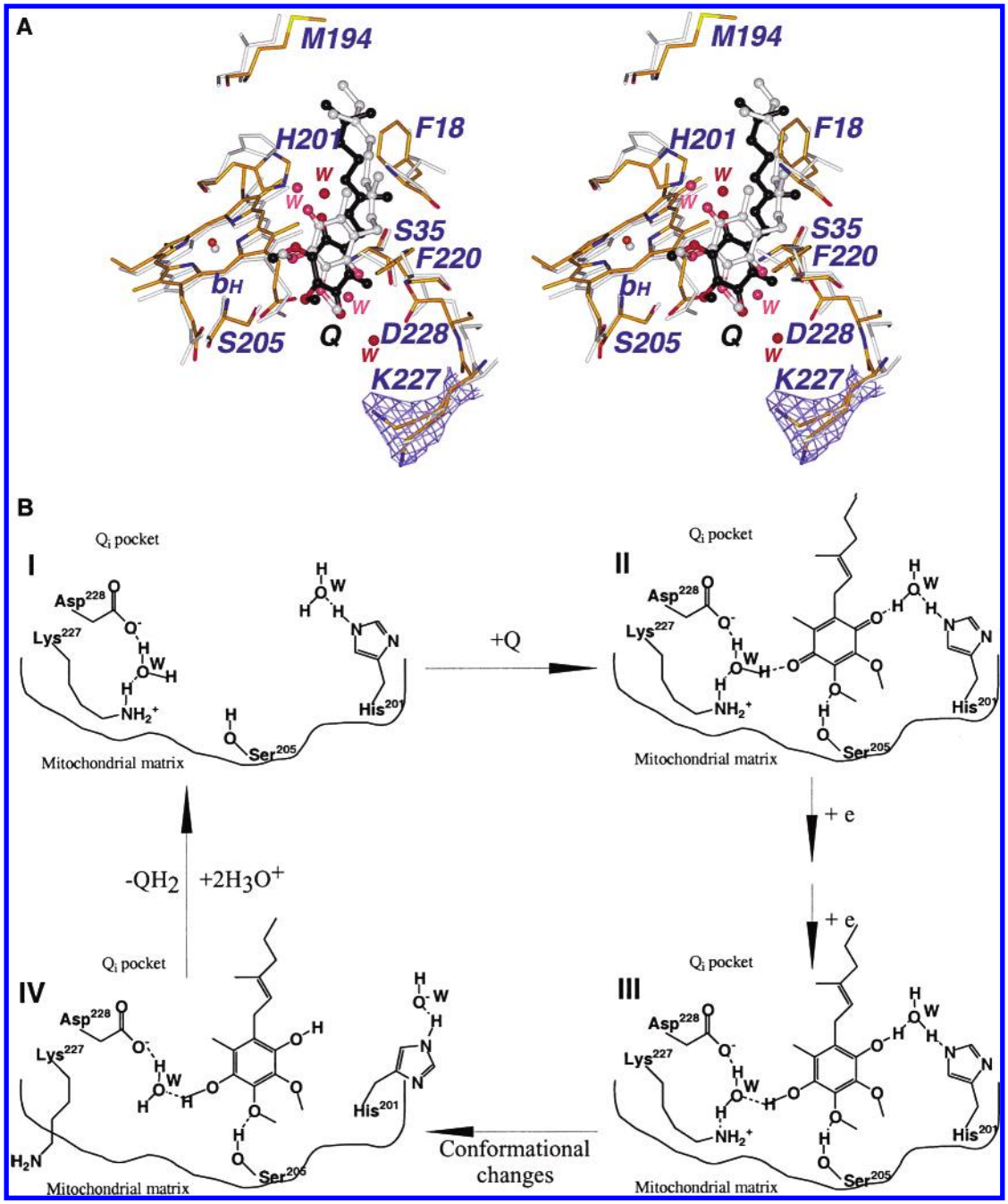

FIGURE 7: Proposed mechanism of ubiquinone reduction reaction at the Q_i site. (A) Structure superposition of residues around the Q_i pocket of the cyt. *b* subunits between bovine and yeast. The bound ubiquinone (Q) in bovine is shown as the ball-and-stick model and color coded with carbon atoms in black, nitrogen in blue, and oxygen in red; the Q interacting residues and the heme b_H are also shown and labeled with an identical color scheme except for the carbon atoms, which are shown in yellow. Equivalent residues and the bound Q6 with truncated isoprenoid repeats in yeast are shown as the ball-and-stick model in gray. Structural water molecules are shown as the isolated balls in red and in magenta for bovine and yeast, respectively. Two alternative conformations for the side chain of Lys^{227} are shown along with the refined $2F_o-F_c$ electron density contoured at 1σ in blue. (B) Schematic diagram showing the proposed mechanism of ubiquinone reduction and protonation. Four residues are shown for the Q_i pocket, which are proposed to play critical roles in the quinone reduction reaction. Conformational changes for His^{201} and Lys^{227} fetching protons from the mitochondrial matrix are indicated; hydrogen and covalent bonding are depicted with dashed and solid lines, respectively.

b_H. When the second electron is delivered to the quinone radical as in the step III of Figure 7B, two protons, each from the respective bound water molecules, are transferred to the phenolic oxygen of the substrate, and His^{201} and Lys^{227} have to give up their respective protons to compensate for the water molecules. Subsequent conformational changes in Lys^{227} and His^{201} (step IV) will take place to allow acquisition of protons from the matrix side. The yeast bc_1 structure would partially represent this conformation.

In the proposed mechanism, the two bound water molecules play crucial roles in substrate binding, proton transfer, and possibly stabilizing the quinone free radical. The water molecule associated with His^{201} is conserved in all refined structures from bovine bc_1 reported here, from the famoxadone bound bc_1 (*9*) and from the yeast (*16*). The water molecule bound with Asp^{228}/Lys^{227} is observed only in the native bc_1 as well as in the one with ubiquinone bound at the Q_i site but expelled upon inhibitor binding. Crystallo-

Table 5: *B* Factors for the Water Molecules Associated with His^{201}, Asp^{228}/Lys^{227}, and Asp^{271}

	B factors (Å^2)		
	His^{201} (Q_i)[a]	Asp^{228}/Lys^{227}(Q_i)	Asp^{271} (Q_o)[a]
native	16 (20)[b]	33 (31)	
ubiquinone	52 (39)	36 (31)	
antimycin A_1	14 (35)		
NQNO1	40 (55)		30 (51)

[a] Q_i and Q_o stand for quinone reduction and quinol oxidation site, respectively. [b] Numbers in parentheses are *B* factors for protein atoms interacting with the bound waters.

graphically, the existence of the water molecules was confirmed by the omit map calculated for the quinone bound bc_1 (Figure 2C); the temperature factors for the bound water molecules are given in Table 5 together with those for the atoms they bind to. It is clear that the magnitude of thermal motion for the water molecules is similar to the atoms in their immediate vicinity.

In addition to the above-mentioned observations that favor the proposed mechanism, it was documented that the ubisemiquinone radical required alkaline pH to be stable in the Q_i site (*47*), consistent with the assumption that both Asp^{228} and His^{201} should be deprotonated. Furthermore, electron nuclear double resonance (ENDOR) experiments showed exchangeable H-bonds to the ubisemiquinone radical (*48*), suggesting that, in our model, the water-mediated H-bonding may be required for stabilizing the free radical. According to this model, the number of H-bonds between the bound ubiquinone and Q_i site residues would be reduced from three to two upon substrate reduction, which would facilitate the product (QH_2) release from the Q_i pocket.

ACKNOWLEDGMENT

The authors wish to thank Dr. Z. Dauter of the X9B beamline at NSLS, BNL; Drs. R. Pahl, J. VonOsinski, and Z. Ren of the BioCARS beamline; and Drs. J. Chrzas of the IMCA beamline at APS, ANL for their assistance in data collection. We thank Dr. M. M. Gottesman of the Laboratory of Cell Biology, NCI, NIH for reading the manuscript.

REFERENCES

1. Hatefi, Y., Haavik, A. G., and Griffiths, D. E. (1962) *J. Biol. Chem. 237*, 1681−1685.
2. Trumpower, B. L., and Gennis, R. B. (1994) *Annu. Rev. Biochem. 63*, 675−716.
3. Brandt, U., and Trumpower, B. (1994) *Crit. Rev. Biochem. Mol. Biol. 29*, 165−197.
4. Trumpower, B. L. (1990) *J. Biol. Chem. 265*, 11409−11412.
5. Mitchell, P. (1976) *J. Theor. Biol. 62*, 327−367.
6. von Jagow, G., and Link, T. A. (1986) *Methods Enzymol. 126*, 253−271.
7. Link, T. A., Haase, U., Brandt, U., and von Jagow, G. (1993) *J. Bioenerg. Biomembr. 25*, 221−232.
8. Kim, H., Xia, D., Yu, C. A., Xia, J. Z., Kachurin, A. M., Zhang, L., Yu, L., and Deisenhofer, J. (1998) *Proc. Natl. Acad. Sci. U.S.A. 95*, 8026−8033.
9. Gao, X., Wen, X., Yu, C., Esser, L., Tsao, S., Quinn, B., Zhang, L., Yu, L., and Xia, D. (2002) *Biochemistry 41*, 11692−11702.
10. Xia, D., Yu, C. A., Kim, H., Xia, J. Z., Kachurin, A. M., Zhang, L., Yu, L., and Deisenhofer, J. (1997) *Science 277*, 60−66.
11. Zhang, Z., Huang, L., Shulmeister, V. M., Chi, Y. I., Kim, K. K., Hung, L. W., Crofts, A. R., Berry, E. A., and Kim, S. H. (1998) *Nature 392*, 677−684.
12. Kim, H., Esser, L., Hossain, M. B., Xia, D., Yu, C. A., Rizo, J., van der Helm, D., and Deisenhofer, J. (1999) *J. Am. Chem. Soc. 121*, 4902−4903.
13. Van Ark, G., and Berden, J. A. (1977) *Biochim. Biophys. Acta 459*, 119−127.
14. Papa, S., Izzo, G., and Guerrieri, F. (1982) *FEBS Lett. 145*, 93−98.
15. Iwata, S., Lee, J. W., Okada, K., Lee, J. K., Iwata, M., Rasmussen, B., Link, T. A., Ramaswamy, S., and Jap, B. K. (1998) *Science 281*, 64−71.
16. Hunte, C., Koepke, J., Lange, C., Rossmanith, T., and Michel, H. (2000) *Structure 15*, 669−684.
17. Lange, C., Nett, J. H., Trumpower, B. L., and Hunte, C. (2001) *EMBO J. 20*, 6591−6600.
18. Yu, C. A., and Yu, L. (1980) *Biochim. Biophys. Acta 591*, 409−420.
19. Yu, C. A., Xia, J. Z., Kachurin, A. M., Yu, L., Xia, D., Kim, H., and Deisenhofer, J. (1996) *Biochim. Biophys. Acta 1275*, 47−53.
20. Xia, D., Kim, H., Yu, C. A., Yu, L., Kachurin, A., Zhang, L., and Deisenhofer, J. (1998) *Biochem. Cell Biol. 76*, 673−679.
21. Otwinowski, Z., and Minor, W. (1997) *Methods Enzymol. 276*, 307−326.
22. CCP4 (1994) *Acta Crystallogr. D50*, 760−763.
23. Murshudov, G. N., Vagin, A. A., and Dodson, E. J. (1997) *Acta Crystallogr. D53*, 240−255.
24. Read, R. J. (1986) *Acta Crystallogr. A42*, 140−149.
25. Jones, T. A., Zou, J. Y., Cowan, S. W., and Kjeldgaard, M. (1991) *Acta Crystallogr. A47*, 110−119.
26. Kraulis, P. J. (1991) *J. Appl. Crystallogr. 24*, 946−950.
27. Esnouf, R. M. (1997) *J. Mol. Graph. 15*, 133−138.
28. Miyoshi, H., Kondo, H., Oritani, T., Saitoh, I., and Iwamura, H. (1991) *FEBS Lett. 292*, 61−63.
29. Tokutake, N., Miyoshi, H., Satoh, T., Hatono, T., and Iwamura, H. (1994) *Biochim. Biophys. Acta 1185*, 271−278.
30. Tokutake, N., Miyoshi, H., Nakazato, H., and Iwamura, H. (1993) *Biochim. Biophys. Acta 1142*, 262−268.
31. Miyoshi, H., Tokutake, N., Imaeda, Y., Akagi, T., and Iwamura, H. (1995) *Biochim. Biophys. Acta 1229*, 149−154.
32. Ballesteros, P., Claramunt, R. M., Canada, T., Foces-Foces, C., Cano, F. H., Elguero, J., and Fruchier, A. (1990) *J. Chem. Soc., Perkin Trans. 2*, 1215−1219.
33. Schnaufer, A., Sbicego, S., and Blum, B. (2000) *Curr. Genet. 37*, 234−241.
34. Weber, S., and Wolf, K. (1988) *FEBS Lett. 237*, 31−34.
35. di Rago, J. P., and Colson, A. (1988) *J. Biol. Chem. 263*, 12564−12570.
36. Coppee, J. Y., Tokutake, N., Marc, D., di Rago, J. P., Miyoshi, H., and Colson, A. M. (1994) *FEBS Lett. 339*, 1−6.
37. Howell, N., and Gilbert, K. (1988) *J. Mol. Biol. 203*, 607−618.
38. Uhrig, J. F., Jakobs, C. U., Majewski, C., and Trebst, A. (1994) *Biochim. Biophys. Acta 1187*, 347−353.
39. Brasseur, G., and Brivet-Chevillotte, P. (1995) *Eur. J. Biochem. 230*, 1118−1124.
40. Yu, C. A., Nagoaka, S., Yu, L., and King, T. E. (1980) *Arch Biochem. Biophys. 204*, 59−70.
41. Takemori, S., and King, T. E. (1964) *J. Biol. Chem. 239*, 3546−3558.
42. Ohnishi, T., and Trumpower, B. L. (1980) *J. Biol. Chem. 255*, 3278−3284.
43. Yu, C. A., Nagaoka, S., Yu, L., and King, T. E. (1978) *Biochem. Biophys. Res. Commun. 82*, 1070−1078.
44. Yu, L., Yang, F. D., and Yu, C. A. (1985) *J. Biol. Chem. 260*, 963−973.
45. Stowell, M. H. B., McPhillips, T. M., Rees, D. C., Soltis, S. M., Abresch, E., and Feher, G. (1997) *Science 276*, 812−816.
46. Hacker, B., Barquera, B., Crofts, A. R., and Gennis, R. B. (1993) *Biochemistry 32*, 4403−4410.
47. Robertson, D. E., Prince, R. C., Bowyer, J. R., Matsuura, K., Dutton, P. L., and Ohnishi, T. (1984) *J. Biol. Chem. 259*, 1758−1763.
48. Salerno, J. C., and Osgood, M. (1990) *Biochemistry 29*, 6987−6993.

49. Brady, G. P., Jr., and Stouten, P. F. W. (2000) *J. Comput.-Aided Mol. Des. 14*, 383−401.
50. Nicholls, A., Sharp, K. A., and Honig, B. (1991) *Proteins: Struct., Funct., Genet. 11*, 281−296.
51. Brasseur, G., Coppee, J., Colson, A., and Brivet-Chevillotte, P. (1995) *J. Biol. Chem. 270*, 29356−29364.
52. Gennis, R. B., Barquera, B., Hacker, B., Van Doren, S. R., Arnaud, S., Crofts, A. R., Davidson, E., Gray, K. A., and Daldal, F. (1993) *J. Bioenerg. Biomembr. 25*, 195−209.

BI0341814